Microstructural Evolution of NF709 Austenitic Stainless Steel Under In-situ Ion Irradiations at Room Temperature, 300, 400, 500 and 600°C

Chi Xu[1,2], Wei-Ying Chen[2], Yiren Chen[2], Yong Yang[1]

[1]*Department of Materials Science and Engineering, University of Florida, Gainesville, FL 32611*
[2]*Nuclear Engineering Division, Argonne National Laboratory, Lemont, IL 60439*

Abstract

Irradiation induced microstructural changes in the NF709 austenitic stainless steel were investigated under 1 MeV Kr ion irradiations at room temperature (RT), 300, 400, 500 and 600°C to different doses. The irradiation-induced defects and the stability of precipitates were characterized with transmission electron microscopy (TEM). Frank dislocation loops were observed in all the irradiated samples, and the loop sizes were much larger at 600°C than those at lower temperatures. "Raft" defect structures, formed through self-alignment of small dislocation loops, were also observed in all irradiated samples. $M_{23}C_6$ precipitates were amorphorized under irradiations at RT and 300°C, but remained to be crystalline at 400°C and above. MX precipitates were stable under irradiations at RT up to 20 dpa, and at temperatures below 600°C to 3 dpa. At 600°C, two MX precipitates were observed to dissolve during in-situ irradiation, suggesting possible precipitate instability at this irradiation temperature.

Keywords: NF709, austenitic stainless steel, in-situ ion irradiation, irradiation microstructure

1. Introduction

The development of sodium-cooled fast reactor (SFR) [1,2] poses significant challenges to the reactor core structural materials, due to the anticipated elevated service temperatures and high fast-neutron fluence [3–5]. The candidate structural materials are required to have an excellent corrosion resistance and irradiation tolerance. An adequate high temperature creep strength is also needed for those candidate materials subjected to mechanical loading at high temperatures. NF709 steel, a 20Cr-25Ni-NbTiN austenitic stainless steel, has been down selected as one of the SFR candidate materials for further assessment based on its overall performance [6]. This alloy was initially developed for the ultra-supercritical power plants, and had shown an excellent creep strength as well as a satisfactory high-temperature corrosion resistance [7,8]. NF709 steel has a unique compositional combination of C and N together with Nb and Ti, which was specially tailored to maintain the material's desired properties over a long term high temperature service through the precipitation of MX type carbo-nitrides [9,10]. Compared with the extensive studies already conducted on the NF709 steel for its phase stability under thermal aging [8,9,11] and corrosion resistance [12], reports on its irradiation response are limited to date and the doses are often limited to a few displacements per atom (dpa) [13]. Long-term neutron-irradiation in a SFR at high temperatures can accelerate the dissolution of existing precipitates and possible nucleation of new types of precipitates in the NF709 steel, which may adversely affect its performance in a reactor [14]. Therefore, it is highly desirable to further evaluate the irradiation stability of the NF709 steel, even at accelerated irradiation conditions, such as the ion-irradiation.

In this study, the NF709 steel samples were in-situ irradiated using 1 MeV Kr ions at temperatures ranging from room temperature (RT) up to 600°C. The irradiation induced defects and stability of the preexisting precipitates were characterized. The objective was to provide a mechanistic understanding on the microstructural evolutions and stability of the precipitates in the NF709 steel under ion irradiations.

2. Experiment

The commercial grade NF709 steel was supplied by the Nippon Steel & Sumitomo Metal Corp., and the as-measured chemical composition is listed in Table 1[13]. The as received material was hot-rolled and then solution annealed at 1200°C for 20 minutes with a final grain size range of 20 - 50 μm. The transmission electron microscope (TEM) disk samples were prepared using a twin-jet electropolisher (Struers® TenuPol-5) with the electrolyte of 5 vol.% perchloric acid in methanol, cooled to around -40°C, and the applied voltage was 27.5 V.

The in-situ ion irradiation experiments were conducted at the Intermediate-Voltage Electron Microscope (IVEM)-Tandem facility at Argonne National Laboratory (ANL). The TEM specimens were irradiated using 1 MeV Kr ions at a flux of 6×10^{11} ions/cm^2/s. The ion beam was at a fixed angle of ~30° to the electron beam, and the samples were tilted towards the ion beam to set an incident angle of around 15°. The ion irradiation dose was calculated using the SRIM [15] (2013 version) with a quick Kinchin-Pease model based method [16]. The calculated dose rate profile in depth is plotted in Fig.1. The irradiation doses were estimated using the average dose through the sample thickness from 0 to ~150 nm.

The specimen numbers and associated irradiation conditions are listed in Table 2. Five specimens (#1-5) were irradiated to ~3 dpa at room temperature (RT), 300, 400, 500 and 600°C, respectively, and one additional specimen (#1') was irradiated up to 20 dpa at RT. After irradiation, the specimens irradiated at 400, 500, and 600°C were cleaned using the Gatan® PIPS II sample cleaning system with low energy (≤ 3 kV) Ar ions at low angles (± 6°). The post-irradiation characterizations were performed on a Philips® CM30T TEM and a FEI® Tecnai F20 TEM, both operated at 200 kV. The diffraction patterns presented in this paper are inverted in black and white for a better clarity.

Table 1. Chemical composition (Wt.%) of NF709 steel.

Cr	Ni	Mo	Mn	Nb	Cu	Si	N	C	Ti	P	B	S	Fe
20.5	25.7	1.52	0.76	0.32	0.365	0.42	0.11	0.076	0.033	0.016	0.0014	0.00001	Bal.

Table 2. List of samples and ion irradiation conditions.

Specimen	Temperature	Fluence ($\times10^{14}$ ions/cm^2)	Dose (dpa)
# 1 & 1'	RT	18.75 & 125	~ 3 & 20
# 2	300°C	18.75	~ 3
# 3	400°C	18.75	~ 3
# 4	500°C	17.6	~ 3
# 5	600°C	18.75	~ 3

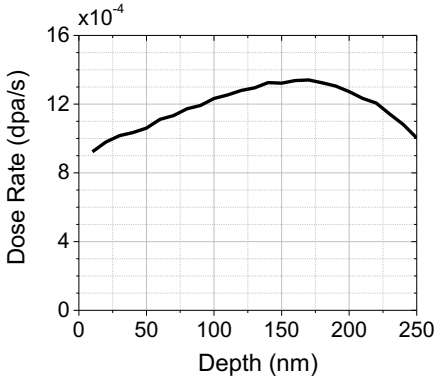

Fig.1. Dose rate profile in the NF709 steel irradiated using 1 MeV Kr ions, calculated using the SRIM 2013 with the Kinchin-Pease model based method.

3. Results

3.1 Characterization of Radiation Induced Defect Structures

3.1.1 In-situ observation of defect evolution

Fig.2 shows the in-situ observation of the defect evolution vs. irradiation dose at room temperature. The weak-beam dark-field (WBDF) images were taken at a condition of (**g**, 3**g**) using **g**{200} near the <011> zone axis. Under the room temperature irradiation, the irradiation mainly introduced small dislocation loops below 1 dpa, while at 3 dpa or above, straight or curly dislocation line segments ("raft" [17,18]) started to evolve as a result of the loop interactions (discussed in 4.2).

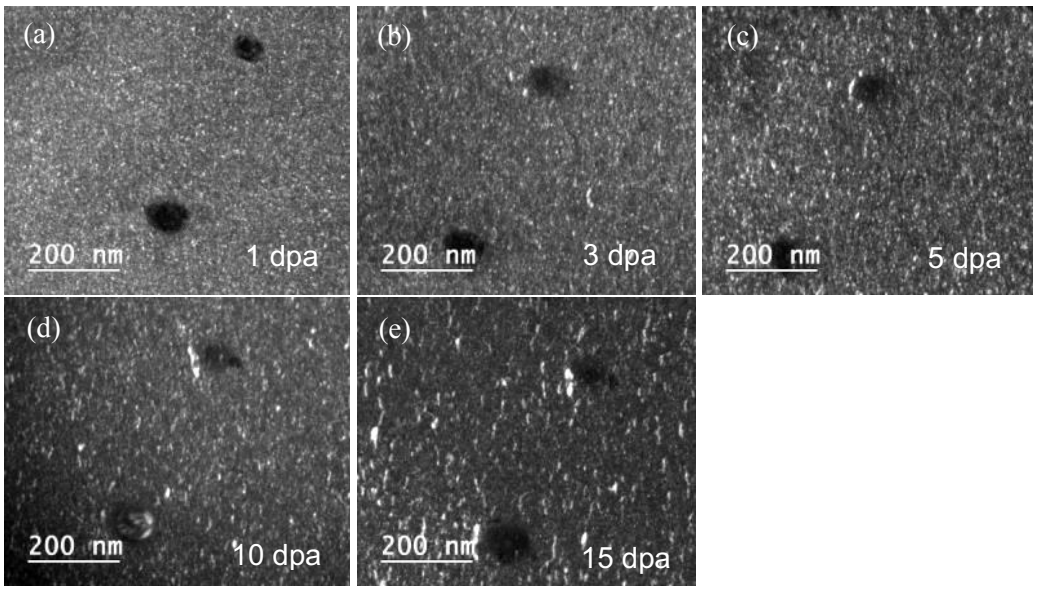

Fig.2. (a-e) WBDF images showing the defect evolutions vs incremental doses in the NF709 steel sample irradiated at RT.

3.1.2 Frank dislocation loops

The irradiation induced Frank dislocation loops were characterized with the rel-rod dark field (RRDF) imaging technique [19]. In this method, the sample is tilted to excite the **g**{311} near the <011> zone axis, and the rel-rod streak showing at between the {111} and {200} diffraction spots is used for dark field imaging. One of the four edge-on Frank loop variants is visible and appear as bright rodlets in the dark field images. Frank loops were observed in the samples irradiated at all five temperatures to 3 dpa. The RRDF images and the corresponding size distributions of the loops are shown in Fig.3 (a) and (b), respectively. The evolution of the mean loop size (diameter) as a function of the irradiation temperature is plotted in Fig.3 (c). The mean loop size increased from ~10 nm to ~30 nm as the irradiation temperature increased from 500°C to 600°C, which is significant.

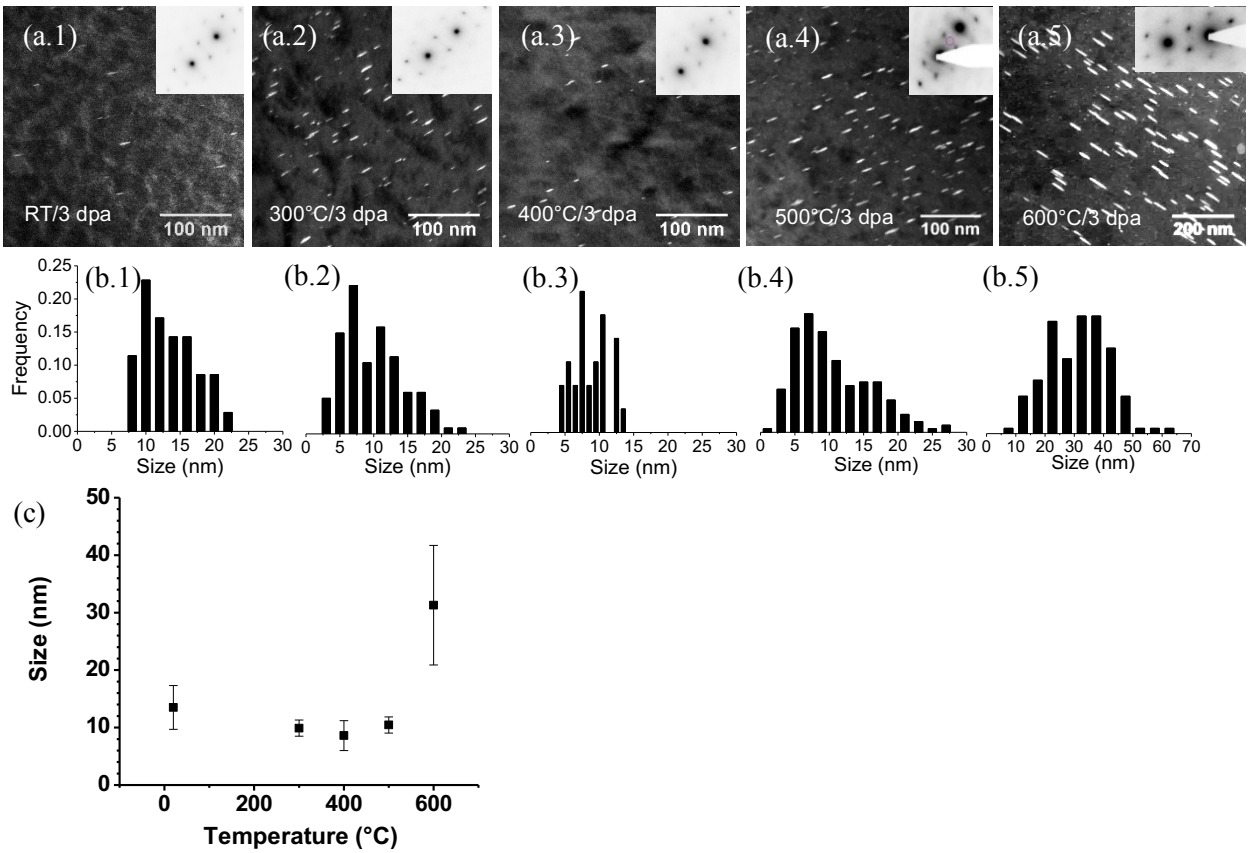

Fig.3. (a.1) - (a.5) RRDF images of Frank loops associated with diffraction patterns for the samples irradiated to 3 dpa at five different temperatures. (b.1) – (b.5) corresponding size distribution histograms. (c) Plot of the mean size of Frank dislocation loops vs. the irradiation temperature, where the error bar shows the standard deviation of the loop size distribution.

3.1.3 The "raft" dislocation structures

As shown in Fig.4, the "raft" dislocation structures ("rafts") were observed at all five irradiation temperatures. They appear as parallel line segments, and separated by defect free regions. The line segments are slightly curled, and they are spaced with a separation ranging from ~20 nm in the RT irradiated specimen to ~60 nm in the 400°C irradiated specimen. It's noted that the TEM observed separation is dependent upon the specimen orientation and volume that contains the "rafts". As shown in Fig.5, the contrasts of the "rafts" were well presented in the 400°C irradiated sample using the reflection of **g**{111}, however, disappeared when using **g**{200}. Instead, isolated Frank dislocation loops were visible (Fig.5 (d)). There are two most commonly observed Burger's vectors for irradiation induced dislocation defects in austenitic steels: **b**=**a**/3<111> and **b**=**a**/2<011> [14,20,21]. In the current case, the possibility of **b**=**a**/3<111> is unlikely, since the **a**/3<111> dislocations are predicted to be visible under the **g**{200} viewing vector (|**g.b**|>0 [22,23]), while they are actually invisible. The "rafts" in this sample are thus suggested to have a Burger's vector of **b**=**a**/2<011>, however, more rigorous tests on dislocation contrast are needed to draw a conclusive statement. As shown in Fig.5, the "rafts" also appear to be parallel to the <200> crystallographic direction, and their density increases with the specimen thickness. The inner details of the "rafts" were further characterized using the WBDF imaging technique, as shown in Fig.6. The zoomed-up insets show that the line segments are composed of discrete bright dots, which are suspected to be the same as the fine-dot defect

clusters in the vicinity of the "rafts". However, it's noted that such "beading" contrasts can also be observed for perfect or partial dislocations in crystalline materials under particular imaging conditions [22].

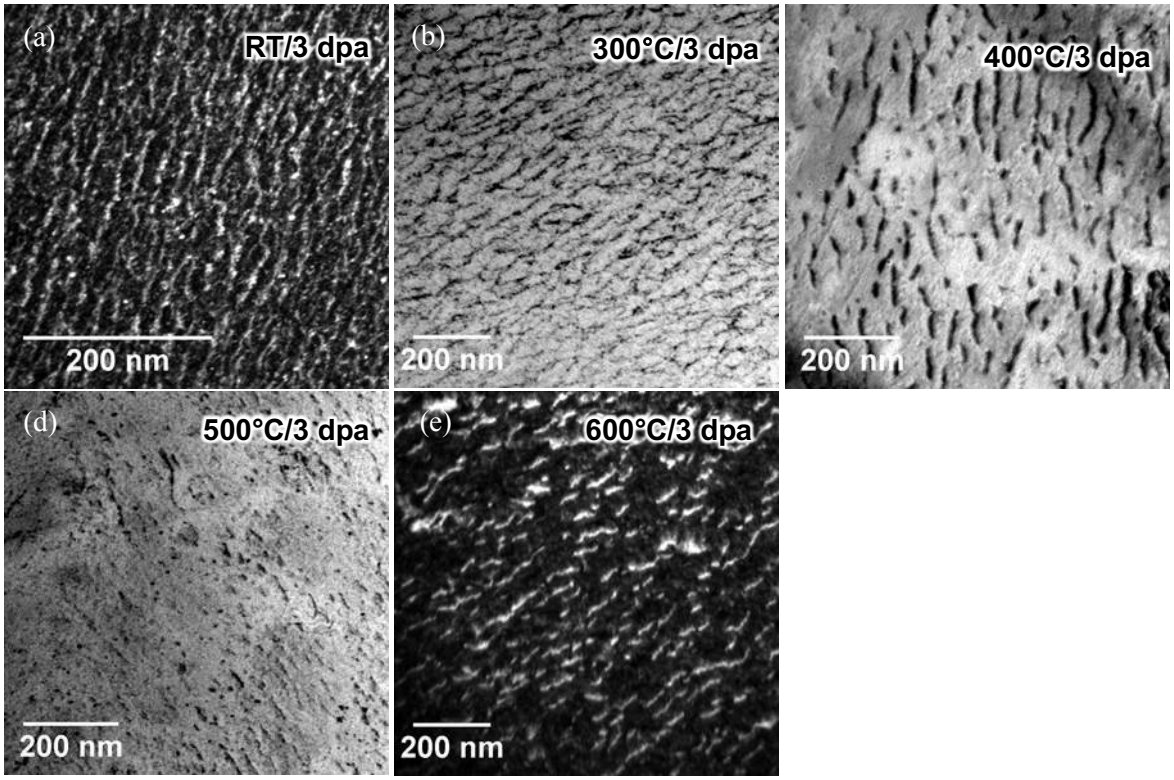

Fig.4. The "rafts" observed in samples irradiated at all five irradiation temperatures: (a) and (e) dark field (DF) images of the samples irradiated at RT and 600°C, respectively. (b), (c) and (d) Bright field (BF) images of the samples irradiated at 300°C, 400°C and 500°C, respectively. .

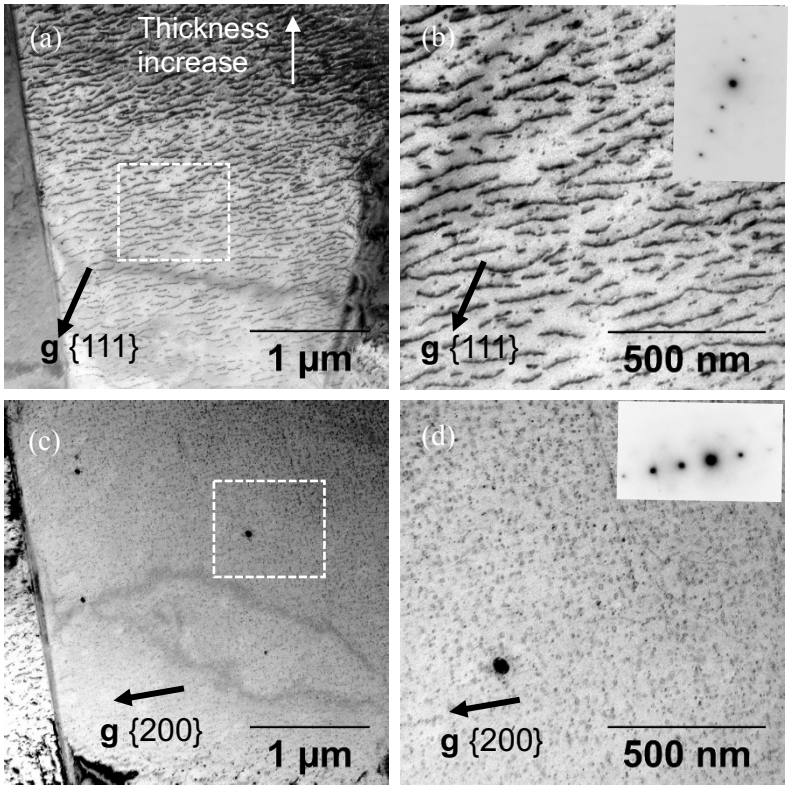

Fig.5. BF images of dislocation structures observed in the 400°C/3 dpa irradiated sample at near the <011> zone axis with diffraction conditions: (a), (b) at (**g**,3**g**) with **g**{111}; and (c), (d) at (**g**,2**g**) with **g**{200}. (b) and (d) are taken from areas highlighted in dashed line squares in (a) and (c), respectively.

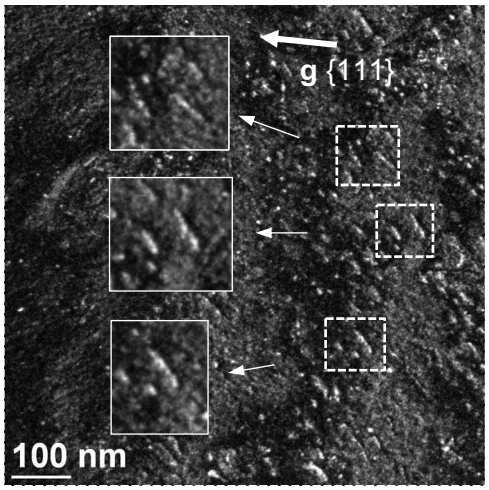

Fig.6. WBDF image of the "rafts" observed in the 500°C/3 dpa irradiated sample, using a diffraction condition of (**g**,5**g**), **g**{111} at near the <011> zone axis. Three blow-up insets show the inner details of the "raft" structures.

3.2 Stability of Precipitates under Irradiation

3.2.1 Pre-existing precipitates

Two types of pre-existing precipitate were identified in the unirradiated NF709 steel: MX (M: Nb, Ti, X: C, N) and Cr rich $M_{23}C_6$ [10]. This result is consistent with the findings reported by Knowles [24] and Powell [25] about the precipitation behavior based on the stabilization ratio (wt.% Nb / wt.% (C+N)) in 20Cr-25Ni steels. As shown in Fig.7, the intragrain $M_{23}C_6$ precipitates have a cuboidal or polyhedron shape with sizes ranging from 100 to 500 nm, and the grain boundary $M_{23}C_6$ precipitates present as rodlets with a diameter of around 50 nm. Some $M_{23}C_6$ precipitates are in a cube-on-cube orientation relationship with the austenite (γ) matrix (Fig.7 (a)). The energy-dispersive X-ray (EDX) spectrum shows Cr enrichment in the selected $M_{23}C_6$ precipitates. The MX precipitates have globular shapes with two different sizes (Fig.7 (c)): the discrete large particles (100 - 200 nm in diameter) and the more densely scattered small particles (~50 nm in diameter), respectively. Some of the small MX precipitates scatter in a lath shaped zone across the grain boundaries, which might be due to the association of MX precipitations with twins or stacking faults [26]. Under certain imaging conditions, the small MX precipitates display a "butterfly-like" contrast with two lobes and a central line of no contrast (Fig.7 (c)). This contrast is normally observed for coherent second-phase particles [22,23], suggesting that the MX precipitates have a coherent interface with the austenite matrix. The EDX spectra shows enrichment of Nb in some MX precipitates (Fig.7 (f)), and enrichment of Nb and Ti in the others, and no distinct morphology differences can be identified between them. As shown in Fig.7, the diffraction patterns from the $M_{23}C_6$ and the MX precipitates are free of extra rings or halo patterns.

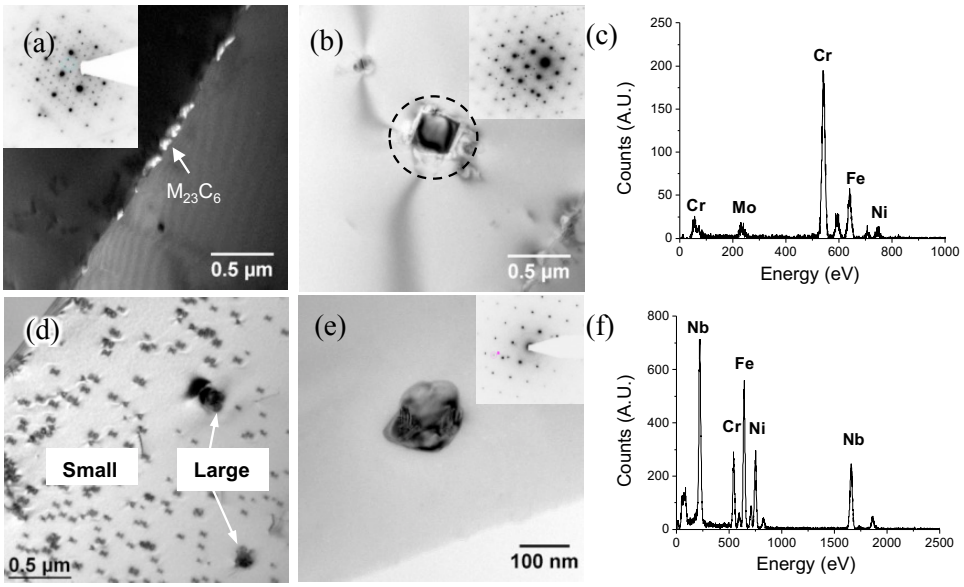

Fig.7. Characterizations of the $M_{23}C_6$ and MX precipitates in unirradiated NF709 steel: (a) DF image and DPs (inset) of $M_{23}C_6$ precipitates at a grain boundary. (b) BF image and DP (inset) of a $M_{23}C_6$ precipitate in the austenite matrix. (c) EDX spectrum from the $M_{23}C_6$ precipitate in (b). (d) and (e) BF images of fine dispersed small MX precipitate and a discrete large MX particle, respectively. (f) EDX spectrum from the large MX precipitates in (d).

3.2.2 Stability of the MX precipitates

As shown in Fig.8 (a), the in-situ observation of a MX precipitate under irradiation (Fig.8 (a)) shows that this individual precipitate has a good stability against irradiation at RT up to 20dpa. The precipitate remains to be crystalline through the irradiation and shows clear diffraction spots, as shown in Fig.8 (b). The MX precipitates also remain crystalline to at least 3 dpa at other irradiation temperatures (300, 400, 500, and 600°C), as shown in the images of Fig.9 (a) – (d) and corresponding DPs. Fig.9 (c) reveals a high

density of irradiation induced defects inside a MX particle irradiated at 500°C to 3 dpa. Another in-situ observation shows that two MX precipitates started to dissolve when being irradiated at 600°C and finally lost their contrasts at ~1.5 dpa, as shown in Fig.10. However, MX precipitates are found to be still existent in the sample after the irradiation and remained to be crystalline, as shown in Fig.9 (d). These results suggest that some of the MX precipitates may become unstable under irradiation at 600°C.

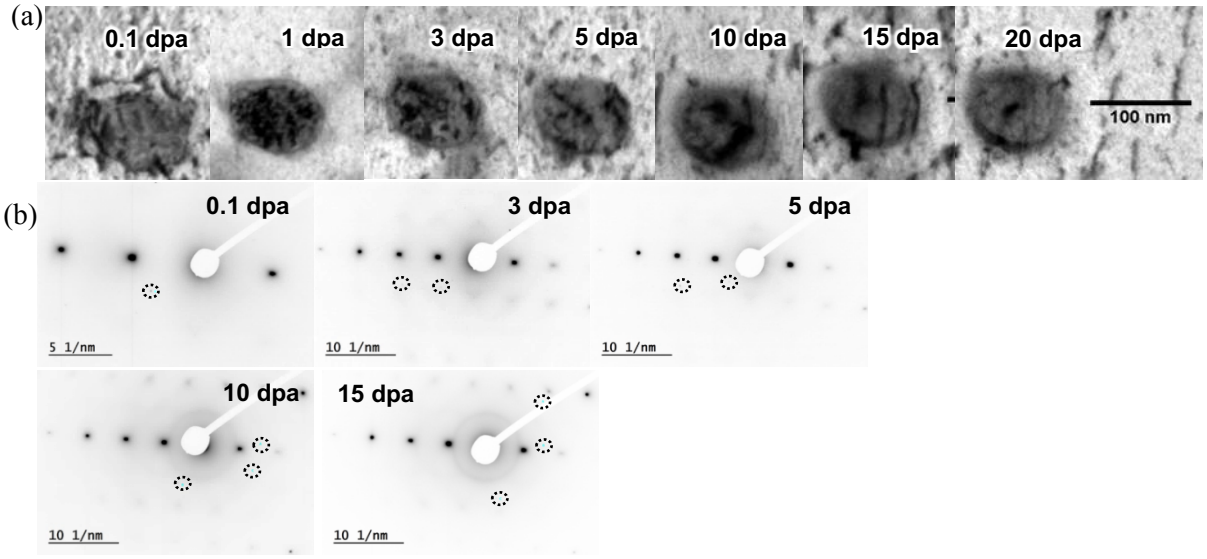

Fig.8. In-situ observation of a MX precipitate under irradiation at RT: (a) a group of BF images with incremental irradiation doses, and (b) corresponding DPs (diffraction spots from the MX precipitate are marked with dashed line circles).

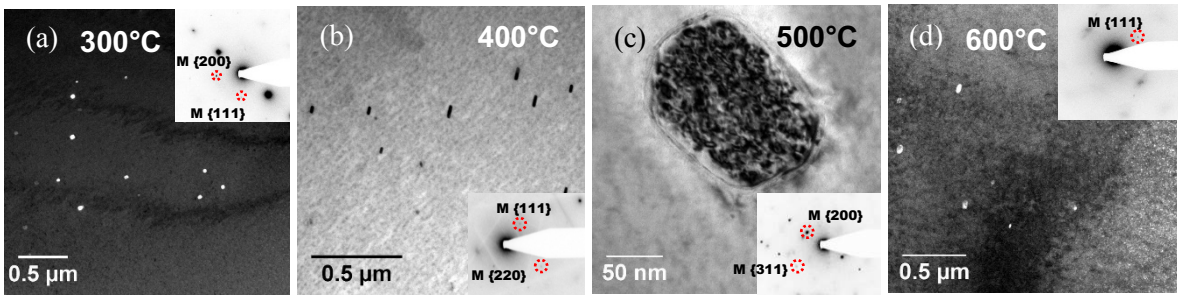

Fig.9. BF and DF images of the MX precipitates in NF709 steel specimens irradiated to a dose of 3 dpa at (a) 300°C, (b) 400°C, (c) 500°C, and (d) 600°C, respectively. The inset DPs show the diffraction spots (highlighted in dashed line circles) from the crystalline MX precipitates ("M" stands for the MX phase).

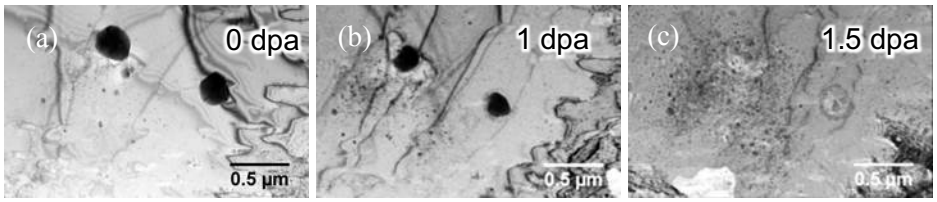

Fig.10. In-situ observation of two MX precipitates dissolving under ion irradiation at 600°C at doses of (a) 0 dpa, (b) 1 dpa and (c) 1.5 dpa.

3.2.3 Stability of the $M_{23}C_6$ precipitates

Examinations of the RT and 300°C irradiated samples indicate that the $M_{23}C_6$ precipitates become amorphous after 3 dpa. As shown in Fig.11 (a), the amorphorized $M_{23}C_6$ precipitates are opaque with no defects observed in these precipitates. In contrast, large numbers of defects were observed in the MX precipitates and the surrounding austenite matrix (Fig.11 (a) and (d)). The amorphization of the $M_{23}C_6$ is evidenced by the diffuse diffraction rings in the DPs. As shown in Fig.11 (b) – (e), the DPs from the $M_{23}C_6$ precipitate show diffuse rings together with diffraction spots while the DPs from the matrix or the MX precipitates only show diffraction spots. The inset DF image in Fig.11(c) taken by selecting part of the ring shows the precipitates enlightened, which confirms that the diffuse rings come from the $M_{23}C_6$ precipitate. Fig.11 (e) shows the amorphization of the grain boundary $M_{23}C_6$ precipitates in the 300°C/3 dpa irradiated sample as well. No diffraction spots belonging to the $M_{23}C_6$ precipitate were observed in any of the DPs, indicating that the $M_{23}C_6$ precipitates had become completely amorphous under the studied irradiation conditions. The EDX results did not reveal any significant composition differences between the amorphorized $M_{23}C_6$ precipitates and those in the unirradiated specimens. The $M_{23}C_6$ precipitates were found to remain crystalline in the samples irradiated at 400°C and above. As shown in Fig.12, there are no diffuse diffraction rings appearing in the DPs from the 400°C/3 dpa or the 500°C/3 dpa irradiated samples. Instead, discrete diffraction spots from the $M_{23}C_6$ precipitates can be clearly identified.

In summary, the stabilities of the $M_{23}C_6$ and MX precipitates under in-situ ion irradiations are concluded in Table 3.

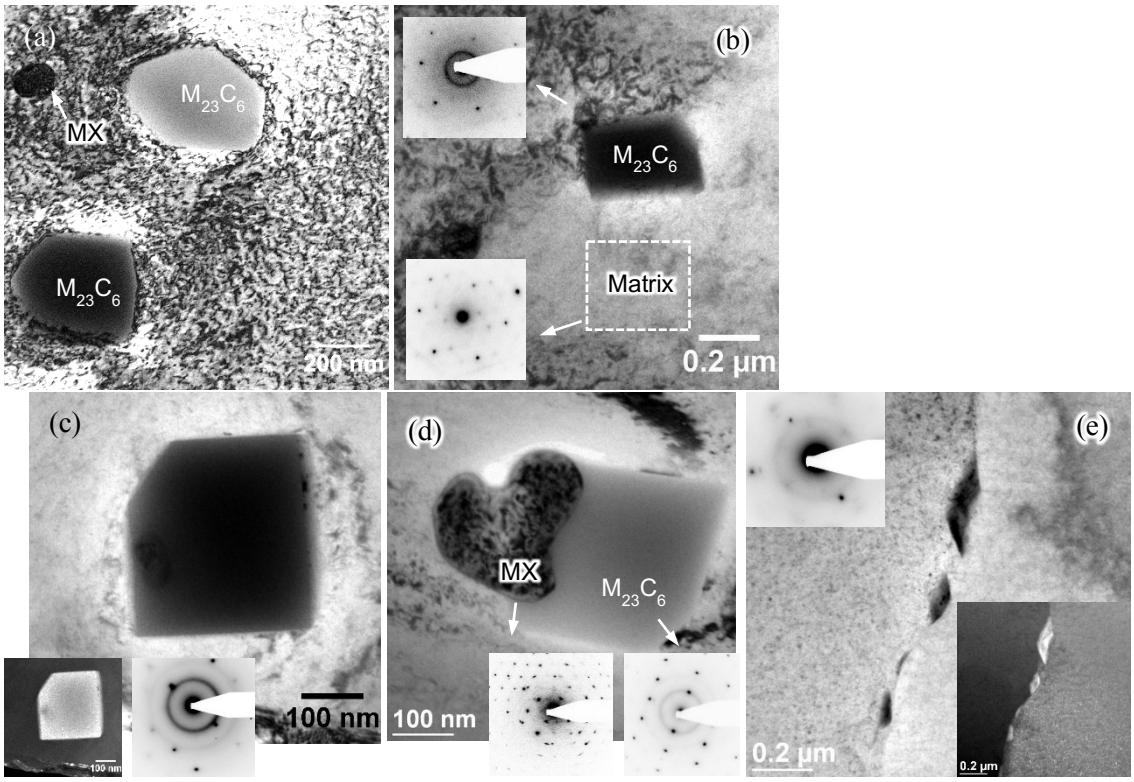

Fig.11. Amorphization of $M_{23}C_6$ precipitates in ion-irradiated NF709 steel. (a, b) BF images showing the amorphous $M_{23}C_6$ precipitates in the (a) RT/3 dpa, and (b) RT/20 dpa specimens. (c - e) BF images showing the amophorized $M_{23}C_6$ precipitates in the 300°C/3 dpa specimen, (e) shows the amorphorized grain-boundary $M_{23}C_6$ precipitates and associated DP on upper left, and DF image on lower right taken using the diffuse ring in the DP.

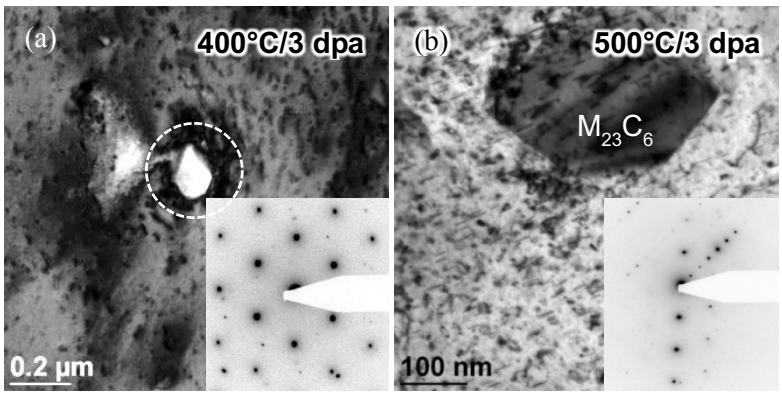

Fig.12. $M_{23}C_6$ precipitates in the NF709 specimens irradiated at (a) 400°C and (b) 500°C. DPs of the precipitates are shown on the lower right of each figure.

Table 3. Summary of the irradiation stabilites of the $M_{23}C_6$ and MX precipitates under the studied irradiation conditions.

Irradiation conditions	$M_{23}C_6$		MX	
	Intra-grain	Grain boundary	Large	Small
Un-irr	√	√	√	√
3 dpa/RT	√ (amo)	?	√	√
3 dpa/300°C	√ (amo)	√ (amo)	√	√
3 dpa/400°C	√	√	√	√
3 dpa/500°C	√	?	√	√
3 dpa/600°C	√	?	√ (insta)	√

√ - exist; × - does not exist; ? - unknown or not measured; (amo) - amorphization observed; (insta) – instability observed.

4. Discussion

4.1 Evolution of Frank Loop Sizes with Irradiation Temperature

As shown in Fig.3, Frank dislocation loops were observed in NF709 samples irradiated at temperatures from RT up to 600°C. Quantifications of the Frank loop sizes shows a well-defined irradiation temperature dependence of the loop mean size at a common dose of 3 dpa, where the mean size slightly decreased from RT to 500°C, but increased significantly from 500°C to 600°C. The significant increase in loop sizes from 500°C to 600°C might be due to a sharp transition of defect cluster evolution kinetics [27,28]. According to Woo and Singh [27], the cascade damages under ion-irradiations introduces an unbalanced production of point defects as well as the defect clusters, termed the "production bias". The irradiation temperature can affect the "production bias" through affecting the vacancy emission rates from vacancy clusters [27]. At low irradiation temperatures, the loop growth is mainly determined by the differences in the sink strengths of dislocations to interstitials and vacancies, known as the "dislocation bias". At close to the peak swelling rate temperature (~ 500℃ [27]), the "production bias" becomes significant, which leaves large amounts of self-interstitial clusters available to the growing dislocation loops and promotes the loop growth significantly [28].

4.2 Formation of the "Rafts"

Irradiation creates a large amounts of point defects and small defect clusters in metallic materials, which further evolve into dislocation loops, dislocation network, voids etc.[20]. Besides the commonly observed defect structures, unique irradiation-induced structures, such as the formation of ordered defect structures, can be formed depending on the irradiated materials and irradiation conditions. Ordered defect structures, e.g. the "raft" structure, are frequently observed in neutron-irradiated metals (Mo, W, Cu, Fe etc. [17,18,29,30]), which appear as dislocation lines decorated with fine-dot shaped defect clusters/loops. Brimhall et al. [18] showed that "rafts" are formed by prismatic glide and self-climb of dislocation loops at intermediate temperatures (400-600°C) in neutron-irradiated Mo. Wen et al. [31] studied the "rafts" in body-centered cubic (BCC) metals using kinetic Monte-Carlo simulations and suggested the formation can be achieved by prismatic glide of glissile interstitial clusters and rotation of their Burger's vectors under the influence of internal strain fields. The periodic defect walls [32], or the ordered arrangements of dislocation loops and cavities [33–35] are often observed in ion-irradiated pure metals, and was thought to be formed in similar mechanisms, i.e. the defect clusters, loops or cavities align in certain crystal orientations (e.g. <200> in Ni [33,35]) to minimize the elastic interaction energy.

The "raft" defect structure observed in our experiment is close in appearance to the observations by Kaoumi et al. [36] and Hernández-Mayoral et al.[37], where the line segments are longer and are more regularly aligned than those reported in other literatures [17,18,29,30]. Kaoumi et al observed the "rafts" (termed as "self-ordered defect structures") during in-situ 1 MeV Kr ion irradiation of the ferritic/martensitic alloys at 20K and 573K [36]. They are shown as parallel line segments with typical separations of 20-50 nm and oriented along the <011> directions in a BCC matrix. The defect clusters that form the "rafts" were observed to jump and move at an irradiation temperature as low as 20K. The movement was attributed to the cascade interactions rather than thermal diffusions. Hernández-Mayoral et al. observed the "rafts" (termed as the "loop strings") in high purity Fe thin foils irradiated with 150 keV Fe^+ ions at RT [37]. Their analysis show that the "rafts" are composed of small **a**/2<111> loops, lining up parallel to the projection of [110] direction in a BCC Fe matrix. The mobile **a**/2<111> loops form an alignment structure, due to the elastic interactions and the reorientation of other loops joining the alignment.

In this study, the "rafts" are suggested to be self-alignments of irradiation induced small dislocation loops, which is supported by the observation (**Error! Reference source not found.**) that the line segments of the "rafts" are composed of fine-dot defect clusters that are essentially small dislocation loops [19]. These small loops are suggested to have a Burger's vector of **a**/2<011> and are aligned along the <200> crystal direction (**Error! Reference source not found.**), which is consistent with the descriptions by Kulcinski et al. [35] for the orientation of loops in the ordered defect structure observed in FCC Ni. The formation mechanism for the self-alignment of the small loops can be explained in the following process [36,37]: the initial dislocation loops formed through cascade damages in the ion-irradiated austenitic steels are of **a**/3<111> sessile characters [19], which change orientations to become glissile through mutual elastic interactions, when the loop density is raised to a high level [31]. The glissile loops pin each other to form line segments. Additional glissile loops will keep joining the line segment to form the "raft" structures.

Deleted:

Deleted:

4.3 Irradiation-induced Amorphization of $M_{23}C_6$ Precipitates

The crystalline-to-amorphous (c-a) phase transition due to energetic particle irradiations at low temperatures is frequently observed in many crystalline materials [38–40]. Specifically, the amorphization of $M_{23}C_6$ precipitates was observed by Sencer et al. [38] in a modified 9Cr-1Mo ferritic/martensitic steel irradiated with proton/neutron mixed spectra. The $M_{23}C_6$ precipitates lost crystallinity and formed diffuse diffraction rings at a dose of 0.5 dpa. Dai et al. [40] also observed the amorphization of the $M_{23}C_6$ precipitates in a martensitic steel (DIN 1.4926) irradiated with 800 MeV protons at temperatures from 50 to 230°C. The amorphization was not completed at 0.4 dpa and fully completed at 3.4 dpa [40]. In both

cases, the compositions of the amorphorized $M_{23}C_6$ precipitates were not significantly changed by the irradiation, and irradiation temperature was critical for the occurance of amorphization. Sencer et al. also showed that the MX precipitates were persistently stable, while the $M_{23}C_6$ precipitates in the same specimens became amorphous [38]. These results are all consistent with the observations in this study.

Two criteria for the amorphization of metal oxides from heavy-ion irradiations were proposed by Naguib and Kelly [41], concerning the ratio of crystallization and melting temperatures and the type of atomic bond. Lam et al. [42–44] proposed a generalized Lindemann melting criterion: the radiation damages are treated as a mean vibration similar to the thermal vibration, and melting happens when the sum of these two vibration terms exceeds a threshold value. It could be told from this theory that the amorphorized materials experience a reduction in the shear modulus ("softening") similar to the thermal heating effect, which potentially affects the mechanical behavior of the material under irradiation. In this study, the c-a transition of the $M_{23}C_6$ precipitates can be explained with a critical damage criterion given by Motta [45], described by the following equation:

$$D(t) = [R - A(T)] \cdot t > D_{critical}$$

where D is the level of lattice disordering and it is a function of time t; R is the displacement rate; A is the annealing rate for the irradiation induced disordering, which is a function of the irradiation temperature T: $A(T) = \sum_i \alpha_i C_i \nu_i \exp(-E_i/kT)$ (i: defect species; C: defect concentration; E: migration energy). The damage yield D must be over a critical level $D_{critical}$ for the c-a transition to happen. It can be told that the annealing rate (A) increases with increasing irradiation temperature (T). At a critical temperature $T_{critical}$ where $R = A(T_{critical})$, the rate of net disordering yield is zero, and the amorphization ($D_t > D_{critical}$) will not take place. This mechanism explains the observation of an upper limit of amorphization temperature, where the amorphization of $M_{23}C_6$ precipitates was not observed at 400°C or above. The critical temperature $T_{critical}$ in the current ion-irradiation experiment is thus determined to be between 300 and 400°C. However, this value is dependent on the displacement rate R, and will be lower at lower displacement rates, such as in a thermal-nuclear reactor. The amorphorized $M_{23}C_6$ precipitate in the RT irradiated sample remained stable up to 20 dpa, showing that the amorphorized phase is stable through accumulating irradiation doses without converting back to the crystalline state. The amorphous phase remains stable to a high irradiation dose over the crystalline phase possibly due to the relaxation of the long-range order constraint by the c-a transition [45].

4.4 Irradiation Stability of the MX Precipitates

The precipitation of fine MX particles is critical for the NF709 steel to achieve and maintain its high creep resistance at high temperatures. The fine MX precipitates serve as obstacles for pinning dislocation motions under creep deformation and defect sinks under irradiations. Therefore, the irradiation stability of the MX precipitates is one of the key factors for the final selection of NF709 as the reactor core structural material in the Gen-IV reactors. Based on the observations in this study, the MX precipitates are stable and remain crystalline structure under the 1 MeV Kr ion irradiations at RT up to 600°C and 3 dpa at least. Considering the high dose rate effect from the heavy ion irradiation, it is anticipated that the MX precipitates would maintain their integrity under a reactor core environment for even higher doses at these temperatures (below 600°C). As our irradiation at 600°C suggested possible instability for some of the MX precipitates, additional experiments are needed to get a complete picture of the irradiation induced instability of the MX precipitates at even higher irradiation temperatures.

4.5 Heavy-ion Irradiation Simulation and the Thin-foil Influences

The use of energetic heavy ions to simulate the cascade damages caused by neutron has shown to be effective [46–48]. The ion-irradiation with in-situ TEM observations method is a valuable technique for studying the irradiation damage mechanisms, which offers the capability of in-situ observation of defect evolutions at well-controlled irradiation conditions [49,50]. The use of 1 MeV Kr ion irradiation was shown to give a similar recoil spectrum for the primary knock-on atoms (PKAs) as the neutrons in a reactor [50]. One of the most common criticisms on this technique is the thin-foil effect, where the free surfaces of the thin foil specimens can serve as defect sinks during irradiation [50], and they might introduce a defect depleted zone near the surface [51]. In this study, the thin foil effect is not considered to have significant impacts on the defect morphology, loop size and precipitate stability results, as these results are determined mechanistically. In fact, no significant differences were identified among regions with different thicknesses regarding these results. The irradiation dose rate used in this experiment is much higher than that in a nuclear reactor, which inevitably affects the defect evolution and precipitate stability of materials in service [47,52,53]. Nevertheless, this paper is focused on the mechanistic studies, additional efforts are required to get an accurate simulation of the materials' irradiation responses in a nuclear reactor.

5. Conclusions

NF709 steel specimens were in-situ irradiated using 1 MeV Kr ions at RT, 300, 400, 500, and 600 °C. The irradiation induced defect structures and the stability of pre-existing precipitates were characterized with TEM. The conclusions are:

- The Frank dislocation loops were quantified using the rel-rod dark field imaging method, and the loop sizes increased significantly at 600°C as compared to those at lower temperatures.
- The "raft" structures were observed in the samples at all irradiation conditions, and they are suggested to be composed of small dislocation loops aligned along the <200> crystal direction with a suggested Burger's vector of **a**/2<011>.
- The $M_{23}C_6$ precipitates became amorphorized under irradiations at RT and 300°C, but remained crystalline structure when irradiated at 400°C or above.
- The MX precipitates were stable under irradiations at RT to 500°C. Possible irradiation induced dissolution was observed during the in-situ irradiation at 600°C.

Acknowledgement

The authors would like to thank Drs. Meimei Li, Marquis A. Kirk, Peter Baldo, and Ed Ryan from the IVEM-Tandem facility, ANL, for their assistance with the in-situ ion-irradiation experiment and for their suggestions in writing this paper. This work was supported by the U.S. Department of Energy, Office of Nuclear Energy, for the Nuclear Energy Enabling Technology (NEET) Program under Contract DE-AC02-06CH11357. The in situ irradiation experiments performed at the IVEM-Tandem facility was supported by U.S. Department of Energy, Office of Nuclear Energy under DOE Idaho Operations Office contract DE-AC07-051D14517 as a part of the Nuclear Science User Facilities (NSUF). Use of the Center for Nanoscale Materials, including resources in the Electron Microscopy Center (EMC), was supported by the U. S. Department of Energy, Office of Science, Office of Basic Energy Sciences, under Contract No. DE-AC02-06CH11357.

References

[1] GIF Portal - Home - Generation IV Systems, (n.d.). https://www.gen-4.org/gif/jcms/c_59461/generation-iv-systems (accessed June 12, 2018).

[2] U.S. DOE, A Technology Roadmap for Generation IV Nuclear Energy Systems, Http://Gif.Inel.Gov/Roadmap/Pdfs/Gen_iv_roadmap.Pdf. (2002). https://ci.nii.ac.jp/naid/10024827101/ (accessed June 12, 2018).

[3] L.. Mansur, A.. Rowcliffe, R.. Nanstad, S.. Zinkle, W.. Corwin, R.. Stoller, Materials needs for fusion, Generation IV fission reactors and spallation neutron sources – similarities and differences, J. Nucl. Mater. 329–333 (2004) 166–172. doi:10.1016/J.JNUCMAT.2004.04.016.

[4] P. Yvon, F. Carré, Structural materials challenges for advanced reactor systems, J. Nucl. Mater. 385 (2009) 217–222. doi:10.1016/j.jnucmat.2008.11.026.

[5] K.L. Murty, I. Charit, Structural materials for Gen-IV nuclear reactors: Challenges and opportunities, J. Nucl. Mater. 383 (2008) 189–195. doi:10.1016/j.jnucmat.2008.08.044.

[6] T.-L. Sham, L. Tan, Y. Yamamoto, Development of Advanced 9Cr Ferritic-Martensitic Steels and Austenitic Stainless Steels for Sodium-Cooled Fast Reactors, International Conference on Fast Reactors and Related Fuel Cycles: Safe Technologies and Sustainable Scenatios (FR13), Paris France, 2013. http://www.iaea.org/inis/collection/NCLCollectionStore/_Public/45/089/45089557.pdf.

[7] H. Naoi, H. Mimura, M. Ohgami, M. Sakakibara, S. Araki, Y. Sogoh, T. Ogawa, H. Sakurai, T. Fujita, development of tubes and pipes for ultra-supercritical thermal power plant boilers, Nippon Steel Tech. Rep. No. 57. (1993) 22–27.

[8] H. Mimura, T. Ishitsuka, Properties of 20Cr-25Ni-Mo-Nb-N Steel Tubes Exposed in Eddystone Unit No.1 Boiler for 75,000 Hours, in: Vol. 9 Eighth Int. Conf. Creep Fatigue Elev. Temp., ASME, 2007: pp. 197–202. doi:10.1115/CREEP2007-26753.

[9] T. Sourmail, H.K.D.H. Bhadeshia, Microstructural evolution in two variants of NF709 at 1023 and 1073 K, Metall. Mater. Trans. A. 36 (2005) 23–34. doi:10.1007/s11661-005-0135-y.

[10] T. Sourmail, Precipitation in creep resistant austenitic stainless steels, Mater. Sci. Technol. 17 (2001) 1–14. doi:10.1179/026708301101508972.

[11] J. Simeg Veternikova, J. Degmova, M. Pekarcikova, F. Simko, M. Petriska, M. Skarba, P. Mikula, M. Pupala, Thermal stability study for candidate stainless steels of GEN IV reactors, Appl. Surf. Sci. 387 (2016) 965–970. doi:10.1016/j.apsusc.2016.06.151.

[12] X. Xu, X. Zhang, G. Chen, Z. Lu, Improvement of high-temperature oxidation resistance and strength in alumina-forming austenitic stainless steels, Mater. Lett. 65 (2011) 3285–3288. doi:10.1016/j.matlet.2011.07.021.

[13] B.K. Kim, L. Tan, C. Xu, Y. Yang, X. Zhang, M. Li, Microstructural evolution of NF709 (20Cr-25Ni-1.5MoNbTiN) under neutron irradiation, J. Nucl. Mater. 470 (2016) 229–235. doi:10.1016/j.jnucmat.2015.12.037.

[14] P.J. Maziasz, Overview of microstructural evolution in neutron-irradiated austenitic stainless steels, J. Nucl. Mater. 205 (1993) 118–145. doi:10.1016/0022-3115(93)90077-C.

[15] J.F. Ziegler, M.D. Ziegler, J.P. Biersack, SRIM – The stopping and range of ions in matter (2010), Nucl. Instruments Methods Phys. Res. Sect. B Beam Interact. with Mater. Atoms. 268 (2010) 1818–1823. doi:10.1016/J.NIMB.2010.02.091.

[16] R.E. Stoller, M.B. Toloczko, G.S. Was, A.G. Certain, S. Dwaraknath, F.A. Garner, On the use of SRIM for computing radiation damage exposure, Nucl. Instruments Methods Phys. Res. Sect. B Beam Interact. with Mater. Atoms. 310 (2013) 75–80. doi:10.1016/J.NIMB.2013.05.008.

[17] B.N. Singh, J.H. Evans, A. Horsewell, P. Toft, G. V Muller, Effects of neutron irradiation on microstructure and deformation behaviour of mono- and polycrystalline molybdenum and its alloys, J. Nucl. Mater. 258 (1998) 865–872. doi:10.1016/S0022-3115(98)00259-1.

[18] J.L. Brimhall, B. Mastel, Neutron irradiated molybdenum-relationship of microstructure to irradiation temperature, Radiat. Eff. 3 (1970) 203–215. doi:10.1080/00337577008236275.

[19] D.J. Edwards, E.P. Simonen, S.M. Bruemmer, Evolution of fine-scale defects in stainless steels

neutron-irradiated at 275 °C, J. Nucl. Mater. 317 (2003) 13–31. doi:10.1016/S0022-3115(03)00002-3.
[20] G.S. Was, Fundamentals of radiation materials science: metals and alloys, Springer-Verlag, 2007.
[21] D.R. Olander, Fundamental Aspects of Nuclear Reactor Fuel Elements, Technical Information Center, Office of Public Affrais, Energy Research and Development Administration, 1976. doi:10.1016/0022-3115(77)90226-4.
[22] J.W. Edington, Practical Electron Microscopy in Materials Science. 3. Interpretation of Transmission Electron Micrographs., Macmillan Press, 1975.
[23] Williams，D.B., C.B. Carter, Transmission Electron Microscopy: a text book for materials science, Springer Scince + Business Media, 2008.
[24] G. Knowels, CEGB Report RD/B/M2419, 1973.
[25] D.J. Powell, R. Pilkington, D.A. Miller, The precipitation characteristics of 20% Cr/25% NiNb stabilised stainless steel, Acta Metall. 36 (1988) 713–724. doi:10.1016/0001-6160(88)90105-8.
[26] W. Kesternich, Dislocation-controlled precipitation of TiC particles and their resistance to coarsening, Philos. Mag. A Phys. Condens. Matter, Struct. Defects Mech. Prop. 52 (1985) 533–548. doi:10.1080/01418618508237645.
[27] C.H. Woo, B.N. Singh, Production bias due to clustering of point defects in irradiation-induced cascades, Philos. Mag. A Phys. Condens. Matter, Struct. Defects Mech. Prop. 65 (1992) 889–912. doi:10.1080/01418619208205596.
[28] C.H. Woo, A.A. Semenov, Dislocation climb and interstitial loop growth under cascade damage irradiation, Philos. Mag. A Phys. Condens. Matter, Struct. Defects Mech. Prop. 67 (1993) 1247–1259. doi:10.1080/01418619308224769.
[29] V.K. Sikka, J. Moteff, “Rafting” in neutron irradiated tungsten, J. Nucl. Mater. 46 (1973) 217–219. doi:10.1016/0022-3115(73)90139-6.
[30] S.J. Zinkle, B.N. Singh, Microstructure of neutron-irradiated iron before and after tensile deformation, J. Nucl. Mater. 351 (2006) 269–284. doi:10.1016/j.jnucmat.2006.02.031.
[31] M. Wen, N.M. Ghoniem, B.N. Singh, Dislocation decoration and raft formation in irradiated materials, Philos. Mag. 85 (2005) 2561–2580. doi:10.1080/14786430500154281.
[32] W. Jäger, P. Erhart, W. Schilling, F. Dworschak, A.A. Gadalla, N. Tsukuda, Periodic {001} walls of defects in proton-irradiated Cu and Ni, Mater. Sci. Forum. 15–18 (1987) 881–888. doi:10.4028/www.scientific.net/MSF.15-18.881.
[33] J.O. Stiegler, K. Farrell, Alignment of dislocation loops in irradiated metals, Scr. Metall. 8 (1974) 651–655. doi:10.1016/0036-9748(74)90015-5.
[34] W. Jäger, H. Trinkaus, Defect ordering in metals under irradiation, J. Nucl. Mater. 205 (1993) 394–410. doi:10.1016/0022-3115(93)90104-7.
[35] G.L. Kulcinski, J.L. Brimhall, Ordered defect structures in irradiated metals, Eff. Radiat. Substruct. Mech. Prop. Met. Alloy. 1973 (1973) 258–271.
[36] D. Kaoumi, J. Adamson, Self-ordered defect structures in two model F/M steels under in situ ion irradiation, J. Nucl. Mater. 448 (2014) 233–238. doi:10.1016/j.jnucmat.2014.01.048.
[37] M. Hernández-Mayoral, Z. Yao, M.L. Jenkins, M.A. Kirk, Heavy-ion irradiations of Fe and Fe--Cr model alloys Part 2: Damage evolution in thin-foils at higher doses, Philos. Mag. 88 (2008) 2881–2897.
[38] B.H. Sencer, F.A. Garner, D.S. Gelles, G.M. Bond, S.A. Maloy, Microstructural evolution in modified 9Cr-1Mo ferritic/martensitic steel irradiated with mixed high-energy proton and neutron spectra at low temperatures, J. Nucl. Mater. 307–311 (2002) 266–271. doi:10.1016/S0022-3115(02)01198-4.
[39] W.J. Weber, R.C. Ewing, L.-M. Wang, The radiation-induced crystalline-to-amorphous transition in zircon, J. Mater. Res. 9 (1994) 688–698. doi:10.1557/JMR.1994.0688.
[40] Y. Dai, S. Bauer, F. Carsughi, H. Ullmaier, S. a Maloy, W.F. Sommer, Microstructure in Martensitic Steel DIN 1 . 4926 after 800 MeV proton irradiation, J. Nucl. Mater. 265 (1999) 203–207.

[41] H.M. Naguib, R. Kelly, Criteria for bombardment-induced structural changes in non-metallic solids, Radiat. Eff. 25 (1975) 1–12. doi:10.1080/00337577508242047.
[42] N.Q. Lam, P.R. Okamoto, M. Li, Disorder-induced amorphization, J. Nucl. Mater. 251 (1997) 89–97. doi:10.1016/S0022-3115(97)00257-2.
[43] F.A. Lindemann, The calculation of molecular Eigen-frequencies, Phys. Z.,(West Ger. 11 (1910) 609–612.
[44] A. Voronel, S. Rabinovich, A. Kisliuk, V. Steinberg, T. Sverbilova, Universality of physical properties of disordered alloys, Phys. Rev. Lett. 60 (1988) 2402.
[45] A.T. Motta, Amorphization of intermetallic compounds under irradiation — A review, J. Nucl. Mater. 244 (1997) 227–250. doi:10.1016/S0022-3115(96)00740-4.
[46] G.S. Was, J.T. Busby, T. Allen, E.A. Kenik, A. Jensson, S.M. Bruemmer, J. Gan, A.D. Edwards, P.M. Scott, P.L. Andreson, Emulation of neutron irradiation effects with protons: Validation of principle, J. Nucl. Mater. 300 (2002) 198–216. doi:10.1016/S0022-3115(01)00751-6.
[47] N.R.T. ASTM, E521 (1996) Standard Practice for Neutron Radiation Damage Simulation by Charged-Particle Irradiation, Annu. B. ASTM Stand. 12 (n.d.).
[48] Z. Jiao, J. Michalicka, G.S. Was, Self-ion emulation of high dose neutron irradiated microstructure in stainless steels, J. Nucl. Mater. 501 (2018) 312–318. doi:10.1016/j.jnucmat.2018.01.054.
[49] M.A. Kirk, P.M. Baldo, A.C.Y. Liu, E.A. Ryan, R.C. Birtcher, Z. Yao, S. Xu, M.L. Jenkins, M. Hernandez-Mayoral, D. Kaoumi, A.T. Motta, In situ transmission electron microscopy and ion irradiation of ferritic materials, Microsc. Res. Tech. 72 (2009) 182–186. doi:10.1002/jemt.20670.
[50] M.A. Kirk, M. Li, D. Xu, B.D. Wirth, Predicting neutron damage using TEM with in situ ion irradiation and computer modeling, J. Nucl. Mater. 498 (2018) 199–212. doi:10.1016/j.jnucmat.2017.10.023.
[51] T. Kimoto, C.W. Allen, L.E. Rehn, Growth rate of dislocation loop in Fe□Ni□Cr alloy under Kr+ ion and electron irradiation, J. Nucl. Mater. 191–194 (1992) 1194–1197. doi:10.1016/0022-3115(92)90663-6.
[52] N. Packan, K. Farrell, J.S.-J. of N. Materials, undefined 1978, Correlation of neutron and heavy-ion damage: I. The influence of dose rate and injected helium on swelling in pure nickel, Elsevier. (n.d.). https://www.sciencedirect.com/science/article/pii/0022311578905135 (accessed June 1, 2018).
[53] E.R. Reese, N. Almirall, T. Yamamoto, S. Tumey, G. Robert Odette, E.A. Marquis, Dose rate dependence of Cr precipitation in an ion-irradiated Fe[sbnd]18Cr alloy, Scr. Mater. 146 (2018) 213–217. doi:10.1016/j.scriptamat.2017.11.040.